Available online at www.sciencedirect.com

ScienceDirect

Journal of the European Ceramic Society 34 (2014) 3051–3059

www.elsevier.com/locate/jeurceramsoc

Microstructure and mechanical properties of $Al_2O_3/Y_3Al_5O_{12}/ZrO_2$ hypereutectic directionally solidified ceramic prepared by laser floating zone

Kan Song [a,b,*], Jun Zhang [b], Xin Lin [b], Lin Liu [b], Weidong Huang [b]

[a] School of Power and Energy, Northwestern Polytechnical University, Xi'an 710072, PR China
[b] State Key Laboratory of Solidification Processing, Northwestern Polytechnical University, Xi'an 710072, PR China

Received 21 November 2013; received in revised form 16 April 2014; accepted 21 April 2014
Available online 14 May 2014

Abstract

$Al_2O_3/Y_3Al_5O_{12}/ZrO_2$ directionally solidified ceramic has been considered as a promising candidate for ultrahigh temperature structural materials due to its excellent performance even close to its melting point. In this work, laser floating zone (LFZ) solidification experiments were performed on $Al_2O_3/Y_3Al_5O_{12}/ZrO_2$ hypereutectic with the solidification rates between 2 μm/s and 30 μm/s. The full eutectic lamellar microstructure is obtained with hypereutectic composition. The solid/liquid interface morphology is investigated. The microstructure characteristic is discussed based on the solid/liquid interface. The variation of lamellar spacing with different compositions and solidification rates was reported and discussed by considering an irregular eutectic growth model. The maximum hardness and fracture toughness are 19.06 GPa and 3.8 MPa $m^{1/2}$, respectively. The toughening mechanism of ZrO_2 is discussed based on the scenario of the crack propagation pattern.

Keywords: Microstructure; Mechanical properties; $Al_2O_3/Y_3Al_5O_{12}/ZrO_2$; Hypereutectic; Directionally solidified ceramic

1. Introduction

$Al_2O_3/Y_3Al_5O_{12}$(YAG)/ZrO_2 directionally solidified ceramic (DSC) has received extensive attention as a new heat-resistant structural material.[1,2] They exhibit a flexural strength of 860 MPa at 1873 K,[3] which is about 57 times higher than that of the sintered ternary composite (approximately 15 MPa) with the same composition and is nearly 2 times larger than that of the *a*-axis sapphire (approximately 450 MPa). Al_2O_3/YAG/ZrO_2 DSC, as a potential replacement for nickel based superalloy, hold a great promise for the development of new generation aero space engine turbine blade. However, an aeroengine working environment simulation indicates that Al_2O_3 phase does not have satisfying corrosion resistance which impedes its potential application.[4] The alumina lamella is prone to be corrupted by water vapor flow with high temperature and velocity.[4] For a long time exposure of Al_2O_3-based DSC in gas turbines, it was proposed that the environmental barrier coatings should be used.[4]

For the improvement the corrosion resistance, refinement of lamellar spacing to prevent the alumina lamella from the corrosion gas flow and decreasing alumina content are also the potential approaches to enhance the corrosion resistance of Al_2O_3-based DSC. The relationships between the average lamellar spacing (λ_{av}) and the solidification rate (V) are compiled in Table 1 (data from[5–13]). Comparing the results from the same preparation method shown in Table 1, it can be concluded that increase of ZrO_2 content leads to the decrease of λ_{av}. Additionally, as shown in Table 1, the increase of ZrO_2 content enhances the fracture toughness of Al_2O_3-based DSC obviously. The experimental evidences illustrate that a decrease of alumina content, refinement of lamellar spacing[14] and strengthening of mechanical property[3] can be achieved simultaneously by increasing an appropriate ZrO_2 content. Therefore, the aim

* Corresponding author at: School of Power and Energy, Northwestern Polytechnical University, Xi'an 710072, PR China. Tel.: +86 29 88494001; fax: +86 29 88494001.
E-mail address: songkan863@mail.nwpu.edu.cn (K. Song).

http://dx.doi.org/10.1016/j.jeurceramsoc.2014.04.033
0955-2219/

Table 1
Lamellar spacing and fracture toughness for the Al_2O_3-based DSC with different compositions and preparation methods.

System	Preparation method	ZrO_2 content (mol%)	$\lambda_{av}V^{1/2}$ ($\mu m^{2/3}\ s^{-1/2}$)	Fracture toughness ($MPa\ m^{1/2}$)
Al_2O_3/YAG eutectic[5]	Modified electron beam floating zone melting	0	6.7	
Al_2O_3/YAG/ZrO_2 eutectic[6]	Modified electron beam floating zone melting	19	5.3	
Al_2O_3/YAG eutectic[7]	μ-PD	0	10	
Al_2O_3/YAG/ZrO_2 eutectic[8]	μ-PD	19	8	
Al_2O_3/YAG eutectic[9]	Laser floating zone	0	10	2–2.4
Al_2O_3/YAG/ZrO_2 eutectic[10]	Laser floating zone	19		4.3
Al_2O_3/YAG eutectic[11]	Laser horizontal zone melting	0		3.6
Al_2O_3/YAG/ZrO_2 hypoeutectic[12]	Laser horizontal zone melting	10		5.2 ± 0.3
Al_2O_3/YAG/ZrO_2 eutectic[13]	Laser horizontal zone melting	18.6		8.0

of this study is, as the further addition of ZrO_2 content, to investigate the microstructure evolution and the mechanical properties of Al_2O_3/YAG/ZrO_2 hypereutectic DSC. Furthermore, the extensive experiments[8,15–21] have been focused on the Al_2O_3/YAG/ZrO_2 eutectic DSC, but the off-eutectic composition was seldom concerned. To date, only a few works[12,14,22–24] focused on the microstructure and the mechanical properties of Al_2O_3/YAG/ZrO_2 off-eutectic DSC. The study on the hypereutectic is significant to clarify the effects of composition on the properties of Al_2O_3-based DSC. The relatively physical parameters of eutectic phases are given in Table 2 (data from[25–27]).

For this purpose, this work is organized according to the following hierarchies. (1) The component phases are clarified to determine whether they are changed by the varied composition. Additionally, it is important to prove whether the primary phase appears. As the boundary conditions for analyzing the eutectic growth can be altered by primary phase, it is meaningless to discuss the relationship between the lamellar spacing and the varied composition when the primary phase exists. (2) The solid/liquid (S/L) interface morphology is a critical basis for the analysis of the as-solidified microstructure formation mechanism. For Al_2O_3/YAG system, the S/L interface morphology was obtained for analyzing growth mechanism of irregular eutectic.[28] In addition, the microstructure formation of growth striation in Al_2O_3/YAG/ZrO_2 DSC was also explained by the S/L interface morphology.[29] Till now, few works[10,29] focused on the S/L interface morphology in Al_2O_3/YAG/ZrO_2 system. In this paper, the S/L interface morphology of Al_2O_3/YAG/ZrO_2 hypereutectic DSC is reported. Furthermore, the microstructure characteristic is discussed based on the S/L interface morphology. (3) Lamellar spacing is an important parameter for characterization of the eutectic microstructure scale. Quantitative lamellar spacing is a key factor and indicator for the understanding of the microstructure evolution. In present work, the variation of lamellar spacing with different compositions and the solidification rates was reported and discussed by considering an irregular eutectic growth model. (4) Finally, the relationship between the mechanical properties of Al_2O_3/YAG/ZrO_2 hypereutectic DSC and ZrO_2 content is given. The toughening mechanism of ZrO_2 is discussed with considering the cracks propagation pattern.

Table 2
Elastic modulus and linear thermal expansion coefficient.

Composition phase	Elastic modulus (E, GPa)	Linear thermal expansion coefficient ($K^{-1} \times 10^{-6}$)
Al_2O_3	390	8.4
YAG	310	8.0
ZrO_2	220	12.65

Data from 25–27.

2. Experimental

2.1. Preparation of the LFZ samples

The chemical compositions of the experimental raw material used in this investigation are listed in Table 3. The ratio of the Al_2O_3 content to Y_2O_3 content is same as that at the ternary eutectic point,[30] the ZrO_2 content was 19.6%, 20.6% and 21.6%, respectively. The different specimens (AYZ1, AYZ2, and AYZ3) used in the experiment are defined in Table 3 and will be referred to in the following discussions. In addition, Al_2O_3/YAG/ZrO_2 ternary eutectic composition, denoted by AYZE, is also listed in Table 3 for comparison.

The raw material was prepared using a mixture of commercial powders of Al_2O_3 (99.99%), Y_2O_3 (99.99%), and ZrO_2 (99.9%). The oxide powders were mechanically mixed by wet ball milling with an aqueous solution of polyvinyl alcohol to obtain a homogeneous slurry and then dried at 473 K in air for 1 h. Afterward, the 68 mm × 4 mm × 4 mm bar precursors were prepared by uniaxial die pressing at 25 MPa for 10 min, and

Table 3
The compositions, volume fraction of the component phases and the elastic modulus of the experimental Al_2O_3/YAG/ZrO_2 DSC used in this investigation.

Symbol	Composition (mol%)			Volume fraction (f, %)			E_C (GPa)
	Al_2O_3	Y_2O_3	ZrO_2	Al_2O_3	YAG	ZrO_2	
AYZE	65.8	15.6	18.6	40	43	17	326.7
AYZ1	65	15.4	19.6	39.5	42.5	18	325.4
AYZ2	64.2	15.2	20.6	39	42	19	324.1
AYZ3	63.4	15	21.6	38.5	41.5	20	322.8

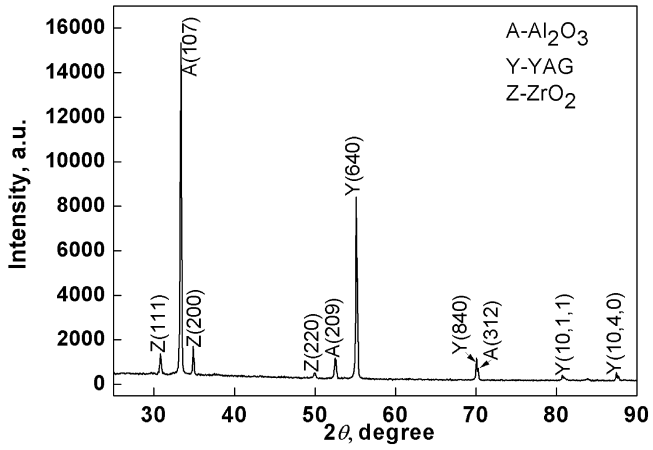

Fig. 1. XRD pattern of the AYZ3 sample.

followed by pressureless sintering at 1673 K for 2 h to increase the density and provide handling strength.

The configuration of LFZ equipment is described elsewhere.[29] The LFZ experiments were carried out with a laser power of 400 W, a solidification rate of 2–30 μm/s and a beam diameter of 4 mm. When the length of directional solidified sample reaches about 5 cm, the laser was abruptly turned off to remain S/L interface.

2.2. Microstructure characterization

The solidified samples were treated by general metallographic analysis methods. The microstructure and component of the composite were determined by scanning electron microscopy (SEM) (JSM-5800), energy dispersive spectroscopy (EDS) (Link-Isis), and X-ray diffraction (XRD) (Rigakumsg-158) technique.

The lamellar spacing was evaluated by scanning the cross-sectional images along a chosen line being perpendicular to most of the phase domains traversed, and then calculating the number of identical pixels in successive segments along the line.[8,28,31,32] The lamellar spacings were measured by repeating at least 400–500 times in the center of the samples. The average lamellar spacing (λ_{av}) is obtained by the arithmetic average of all of the measured values.

2.3. Mechanical tests

Because the LFZ samples are not large enough for conventional, macroscopic fracture toughness tests, the hardness and

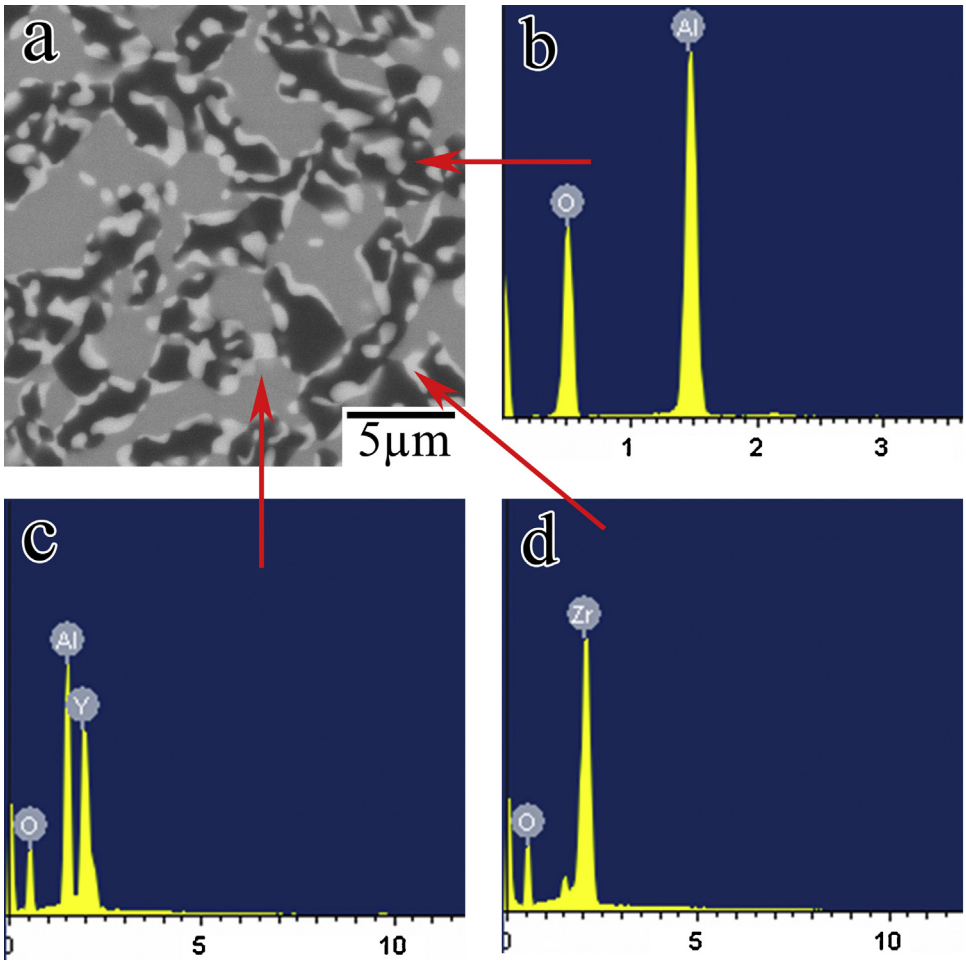

Fig. 2. The typical transverse section microstructure of AYZ3 sample (a) and the corresponding EDS analysis of the component phases (b–d).

fracture toughness are measured on the polished surface of the samples at room temperature by using the Vickers indentation technique following the ASTM C1327-99 standard. The indentations were made using 9.8 N loads for 15 s, and at least ten valid microindentations were conducted in each sample. The hardness and fracture toughness are calculated according to the following equations proposed by Niihara[33] for Palmqvist cracks:

$$Hv = 1.8544 \cdot \frac{P}{a^2} \quad (1)$$

$$K_{IC} = 0.016 \cdot \left(\frac{E_C}{Hv}\right)^{2/5} \left(\frac{P}{al^{1/2}}\right) \quad (2)$$

where Hv is the Vickers hardness, K_{IC} the fracture toughness, E_C the elastic modulus of the ceramic, P the indentation load, a half the indentation diagonal, and l is the crack length. This method is simple, convenient, nondestructive and low-cost to evaluate the hardness and fracture toughness of small and relatively brittle specimens. Such technique has received great attention in recent years for measuring the mechanical properties of oxide DSC with a small volume.[10,15]

3. Results and discussion

3.1. Constituent phase analysis

The XRD (Fig. 1) analysis carried out from AYZ3 sample shows that the hypereutectic microstructure is only composed of Al_2O_3, YAG and ZrO_2 phases without any other phases. Fig. 2 shows the typical transverse section microstructure (Fig. 2a) and EDS analysis of the phases with different colors (Fig. 2b–d). It indicates that the black zone is Al_2O_3 phase (Fig. 2b), the gray zone is the YAG phase (Fig. 2c), and the fine white zone is the ZrO_2 phase (Fig. 2d). The experimental results of constituent phase analysis are consistent with that carried out from ternary eutectic composition[10,15,34] and indicate that the constituent phase is not changed by the variation of the raw material composition. Additionally, the primary phase with dendrite morphology is not observed from Fig. 2a.

3.2. S/L interface morphology and typical microstructure

Fig. 3a shows the S/L interface morphology of AYZ3 sample solidified with a rate of 2 μm/s. The YAG phase, coupled with ZrO_2 phase, is being projected into the melt and plays the leading role in the ternary eutectic solidification. In addition, the primary phase, which grows as a dendritic morphology, is not observed from the S/L interface (Fig. 3a). It can be concluded that a full lamellar microstructure is achieved in hypereutectic composition by using LFZ method. The interface morphology is same as the result carried out at ternary eutectic composition,[10,34] and is considered as a result of the high entropy of melt of YAG.[10] Such phenomenon can also be explained by analyzing growth undercooling. In the Al_2O_3/YAG/ZrO_2 ternary system, YAG and ZrO_2 dissolve each other,[30] but it was confirmed that the absence of Al_2O_3 solubility in solid solutions YAG and ZrO_2.[30,35] This suggests that YAG phase and ZrO_2 phase exhibit a coupled growth

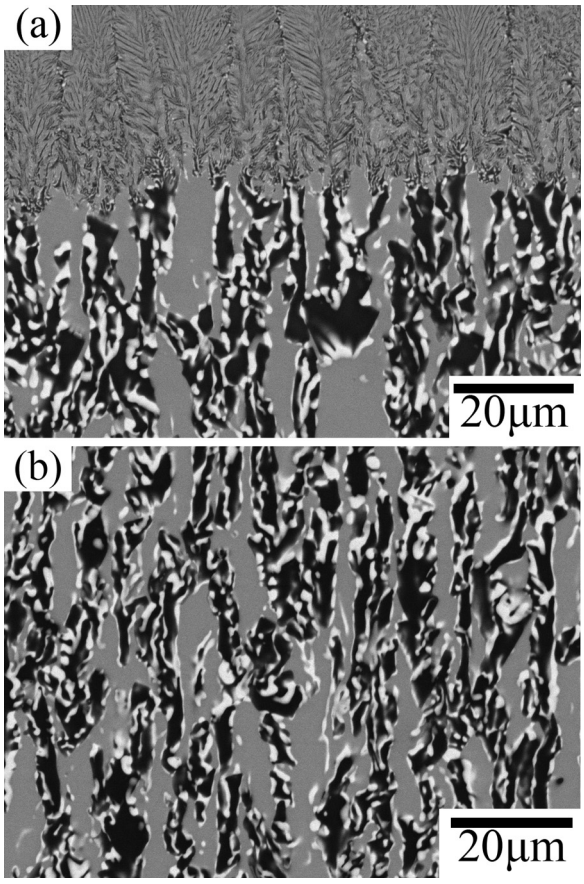

Fig. 3. S/L interface morphology (a) and the longitudinal section microstructure (b) of the AYZ3 sample grown at the solidification rate of 2 μm/s.

mechanism through a diffusion couple. The solute undercooling of YAG phase and ZrO_2 phase is reasonably decreased.[36] Furthermore, according to an equilibrium phase diagram,[30] the temperature of binary eutectic point in YAG/ZrO_2 system is higher than that in Al_2O_3/YAG system. Therefore, YAG phase and ZrO_2 phase coupled each other and play a leading role in the growth of Al_2O_3/YAG/ZrO_2 ternary hypereutectic system.

Fig. 3b shows the typical microstructure of Al_2O_3/YAG/ZrO_2 ternary hypereutectic obtained from the longitudinal section. The YAG phase and Al_2O_3 phase with similar sizes are interweaved with each other; while the much smaller ZrO_2 phase is either distributed as slices at the interface between Al_2O_3 and YAG phases or scattered as rods in the Al_2O_3 phase. The volume fractions of three component phases measured from different samples are shown in Table 3.

3.3. Average lamellar spacing

Fig. 4(a–c) shows the microstructure obtained from transverse section of AYZ2 sample with solidification rate less than or equal to 8 μm/s. The measured average lamellar spacing of AYZE and AYZ2 sample is shown in Fig. 4d. It indicates that, for AYZ2 sample, the lamellar spacing is larger than AYZE samples grown at the same rate. But the situation is reversed in high solidification rate (30 μm/s). Fig. 5(a–c) shows the microstructure obtained from transverse section of Al_2O_3/YAG/ZrO_2 DSC as

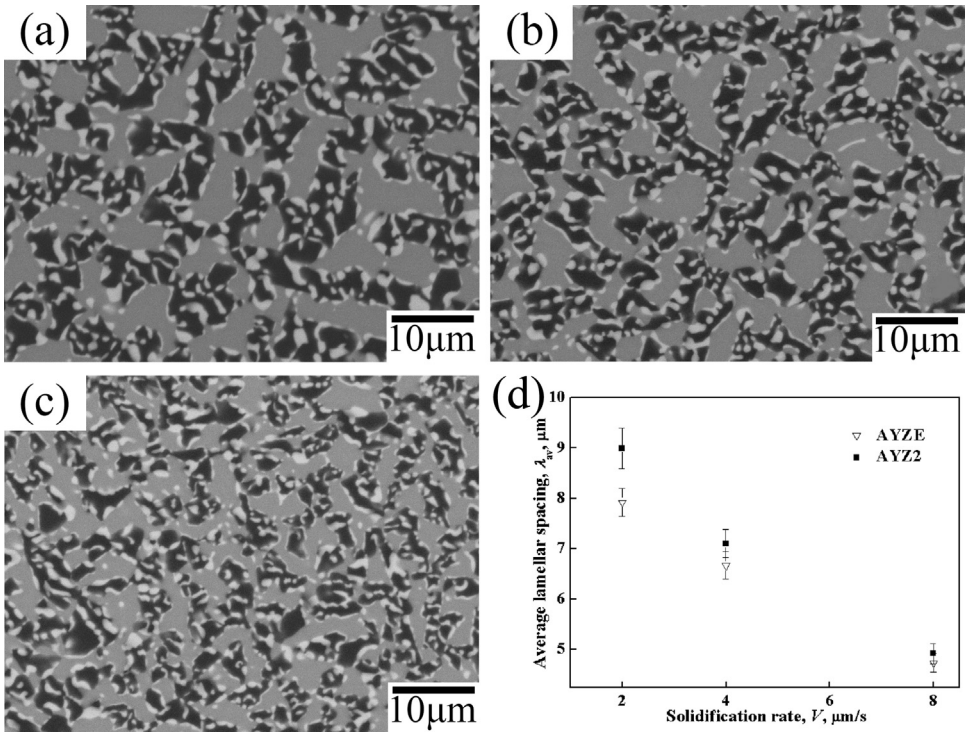

Fig. 4. The microstructure of AYZ2 sample at the different solidification rates: (a) $V = 2$ μm/s, (b) $V = 4$ μm/s, (c) $V = 8$ μm/s, and (d) measured average lamellar spacings (λ_{av}) of AYZE and AYZ2 samples as a function of solidification rate.

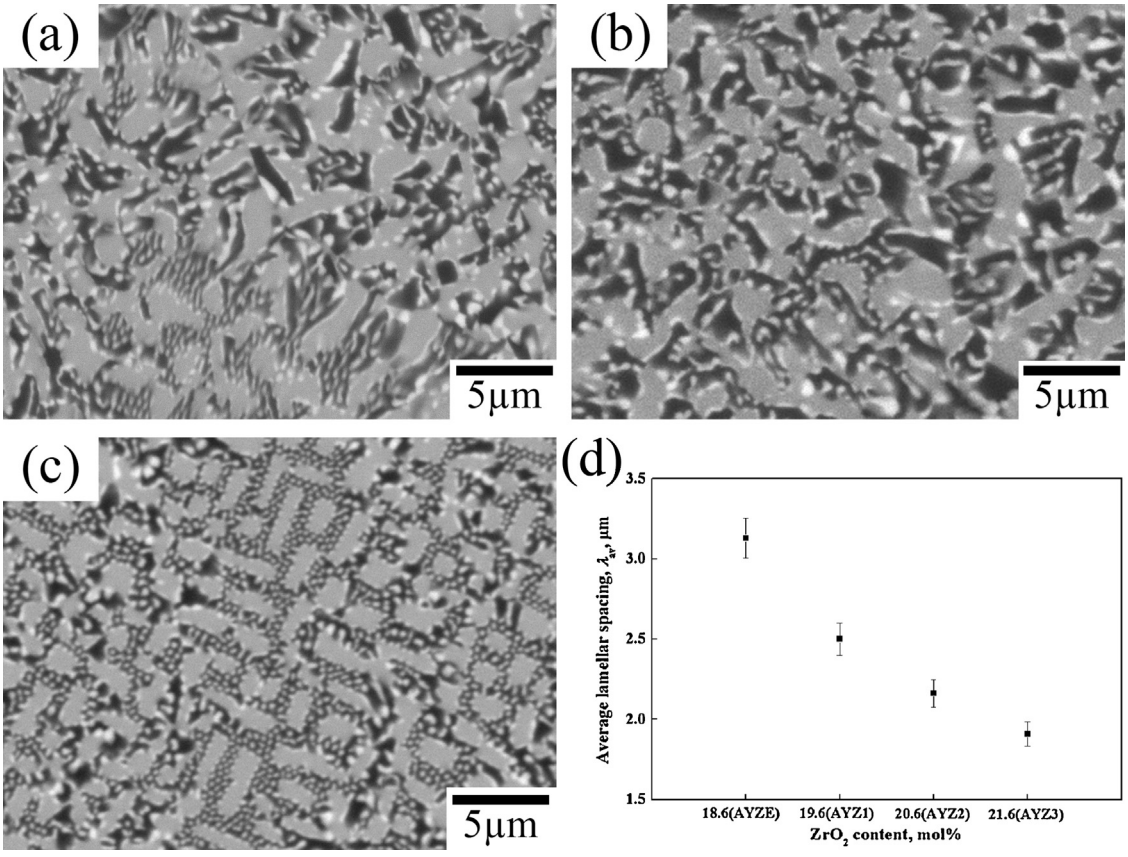

Fig. 5. The microstructure of Al_2O_3/YAG/ZrO_2 DSC with the different ZrO_2 content (mol%) at the solidification rate of 30 μm/s: (a) mol% = 19.6%, (b) mol% = 20.6%, (c) mol% = 21.6%, and (d) measured average lamellar spacings (λ_{av}) as a function of ZrO_2 content at the solidification rate of 30 μm/s.

a function of ZrO_2 content at the solidification rate of 30 μm/s. The measured average lamellar spacing is given in Fig. 5d. It indicates that the lamellar spacing decreases with an increase of ZrO_2 content at that higher solidification rate. The observed minimum lamellar spacing is 1.9 μm, which occurs in AYZ3 sample. The microstructure evolution can be explained from the heat and mass transfer as below.

Firstly, the lamellar spacing of irregular eutectic is strongly affected by the heat transfer as well as the temperature gradient (G) in the front of S/L interface.[37–42] G is a function with thermal conductivity, k. The expression of the temperature gradient was derived based on the assumption of the uniform heat flow from the melt to the solid phase.[43] The uniform heat flow is the common feature in the directional solidification process including the laser floating zone. Hence, this model can be used to evaluate the thermal field near the solid/liquid interface and the temperature gradient in directional solidification process.[43] The expression of G can be defined as:[43]

$$G = \frac{1}{k_l}\left[\frac{2h(T_m - T_0)k_s}{Vr\rho_s C_p} - \rho_s L V\right] \tag{3}$$

with the following parameters: T_m and T_0 are the temperature of melt point and room-temperature, respectively. h is a combined coefficient of heat transfer. r is the radius of sample. ρ and C_p are the density and specific heat, respectively. L is the latent heat. The subscripts s and l represent solid and liquid phase, respectively. From the above formula, it indicates that a low k_s leads to a decrease of the temperature gradient. ZrO_2 possesses a much lower thermal conductivity (2.5 W/m k) compared with the Al_2O_3 (10 W/m k) and YAG (10 W/m k). Thus the thermal conductivity of the solidified sample and the temperature gradient decrease with increase of content of ZrO_2.

Secondly, the lamellar spacing is also affected by the mass transfer as well as the diffusion coefficient (D_L) in the liquid. The diffusion coefficient decreases with an increase of ZrO_2 content.[12,22]

From the above analysis, it can be conclude that the increase of ZrO_2 content leads to the decrease of the temperature gradient and the diffusion coefficient synchronously. However, the effects of the two factors on the lamellar spacing are completely opposite. The decrease of the temperature gradient and the diffusion coefficient result in the increase[44,45] and decrease[36,46] of the lamellar spacing, respectively. For analyzing the relationship between the lamellar spacing and the two factors synthetically, the formation mechanism of the irregular eutectic must be reviewed.

Fig. 6 shows the formation mechanism of the irregular eutectic schematically. The scales of irregular eutectic microstructure are directly governed by branching and ceasing of the facet lamellae.[40] The different facet lamellas (β phase in Fig. 6) have their own preferred growth orientations which differ from the uniform heat-flow induced by directional solidification method. When the two lamellae converge, the lamellar spacing decreases to λ_{min}.[42,45] The spacing cannot further reduce since this will lead to the sharp increase of undercooling. In this case, the growth of one phase simply stops, thereby increasing the

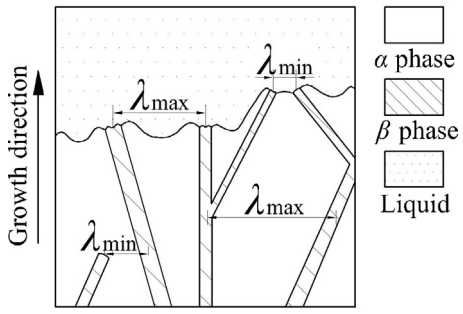

Fig. 6. Schematic diagram of the longitudinal section of irregular eutectic.

spacing. Therefore, λ_{min} was considered as the minimum lamellar spacing and can be expressed as:[36]

$$\lambda_{min} = \left[\frac{2D_L}{C_0 PV}\left(f_\beta \frac{\Gamma_\alpha \sin\theta_\alpha}{|m_\alpha|} + f_\alpha \frac{\Gamma_\beta \sin\theta_\beta}{m_\beta}\right)\right]^{1/2}$$
$$P = \sum_{n=1}^{\infty}\frac{1}{(n\pi)^3}\sin^2(n\pi f_\alpha) = \sum_{n=1}^{\infty}\frac{1}{(n\pi)^3}\sin^2(n\pi f_\beta) \tag{4}$$

where Γ is the Gibbs–Thomson coefficient, f is the volume fraction, m is the liquidus slope. θ is the contact angle imposed by the surface tension balance at the three phase junction. C_0 is the length of the eutectic tie-line. The subscripts α and β represent α and β phase, respectively.

Conversely, when the lamellar spacing is much larger, a solute enrichment at the S/L interface leads to the branching of the lamellae contributed by the high constitutional undercooling. The branching value is considered as the maximum lamellar spacing and denoted by λ_{max}. The classic expression of λ_{max} was derived by Magnin and Kurz[47] and given as:

$$\lambda_{max} = \left(\frac{2\Gamma_{\chi F}[2+\cos(\theta_{\chi F})]}{f_{\chi F}\left(\frac{|m_{\chi F}|C_0}{D_L\tan(\theta_{\chi F})}\left(\Pi_{\chi F} - \frac{P}{f_{\chi F}}\right)V + \frac{f_{\chi F}}{24}G\right)}\right)^{1/2}$$
$$\Pi_\chi = \sum_{n=1}^{\infty}\frac{1}{(n\pi)^2}\sin(n\pi f_\chi) \quad \chi = \alpha, \beta \tag{5}$$

where χF represent facet phase. Furthermore, Trivedi et al.[39] suggest that the average lamellar spacing can be obtained by the arithmetical mean of branching value and ceasing value of eutectic lamellar. Therefore, the average lamellar spacing (λ_{av}) of irregular eutectic can be given by:

$$\lambda_{av} = \frac{\lambda_{min} + \lambda_{max}}{2} \tag{6}$$

Eqs. (4)–(6) indicate that the lamellar spacing of irregular eutectic is affected by both of the temperature gradient and the ratio of solidification rate to diffusion coefficient in liquid (V/D_L).[36] An increase of either of the G or V/D_L induces the decrease of lamellar spacing. Furthermore, the effect of G on the lamellar spacing is not correlated to the solidification rate, but the impact of V/D_L against lamellar spacing is related to the solidification rate. In another words, which condition dominates the competition depends on the range of the solidification

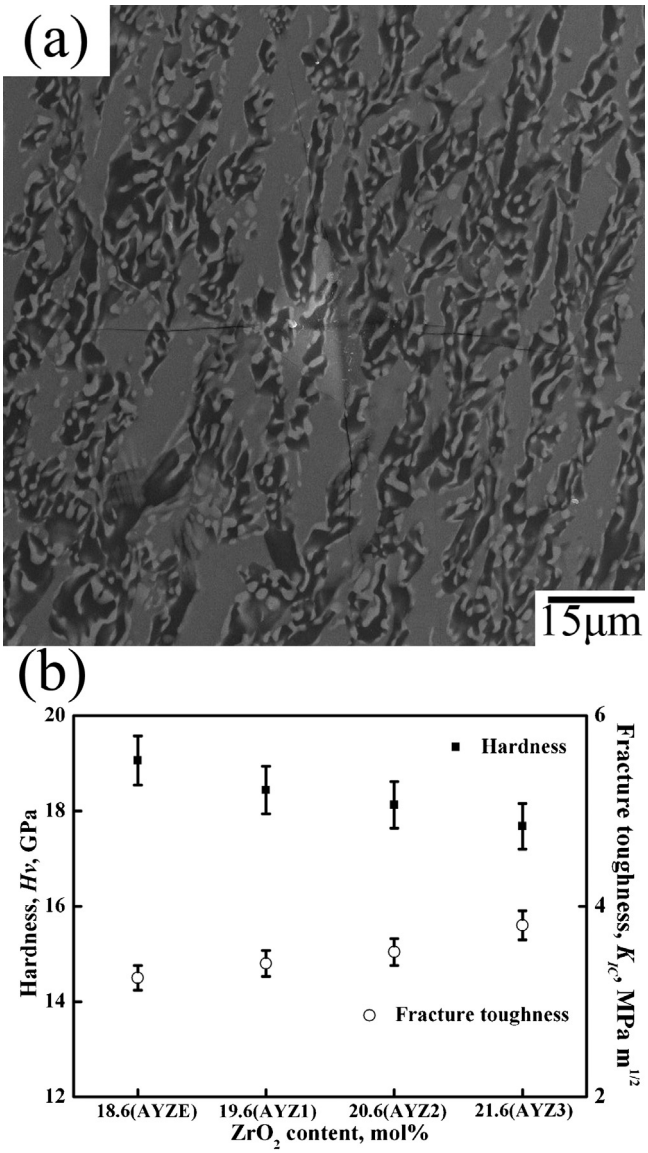

Fig. 7. Vickers indentation morphology on the polished surface of the Al_2O_3/YAG/ZrO_2 DSC (a) and the dependence of the hardness and fracture toughness of Al_2O_3/YAG/ZrO_2 DSC (V = 2 μm/s) as a function of ZrO_2 content (b).

rate. At a low solidification rate, the lamellar spacing is sensitive to the variation of G. Therefore, the AYZ2 samples, which possess lower temperature gradient, have a relatively larger lamellar spacing than the AYZE samples. On the other hand, V/D_L becomes the predominant factor to affect the irregular eutectic lamellar spacing for a higher solidification rate. Hence, at higher solidification rates, the lamellar spacing decreases with the increase of the ZrO_2 content which reduces the diffusion coefficient.

3.4. Hardness and fracture toughness

The typical indentation crack on the polished surface is shown as Fig. 7a. The hardness measured on the Al_2O_3/YAG/ZrO_2 DSC solidified at the rate of 2 μm/s is plotted in Fig. 7b as a function of ZrO_2 content. The maximum hardness is 19.06 GPa obtained from the AYZE sample. This value is higher than that reported on Al_2O_3/YAG/ZrO_2 ternary eutectic fiber prepared by LFZ method (14.8 GPa)[10] and slightly lower than that prepared by optical floating zone method (19.8 GPa).[48]

For the calculation of the fracture toughness, the elastic modulus of the Al_2O_3/YAG/ZrO_2 DSC is needed in Eq. (2). In this paper, the elastic modulus of composites (E_C) was calculated by Halpin–Tsai equation:[49]

$$E_C = E_{Al_2O_3} f_{Al_2O_3} + E_{YAG} f_{YAG} + E_{ZrO_2} f_{ZrO_2} \quad (7)$$

The elastic modulus of the composition phases is given in Table 2. The calculated elastic modulus of Al_2O_3/YAG/ZrO_2 DSC with different composition is shown in Table 3. Further, the fracture toughness is also plotted in Fig. 7b. The results exhibit a noticeable enhancement of fracture toughness as ZrO_2 content increased. The maximum of the fracture toughness is 3.8 MPa $m^{1/2}$. Additionally, the fracture toughness in this work is obviously higher than that obtained from Al_2O_3/YAG eutectic fiber manufactured by the analogous LFZ method (2–2.4 MPa $m^{1/2}$).[9] It illustrates ZrO_2 plays a role on the toughening the Al_2O_3-based DSC.

It is widely recognized that the toughening effect of ZrO_2 arises from the discrepancy in the thermal expansion coefficients of the ZrO_2, YAG and Al_2O_3 phases as shown in Table 2. Because Al_2O_3 and YAG phases have similar thermal expansion coefficients, the residual stresses are almost free in Al_2O_3/YAG binary eutectic. However, the thermal expansion coefficient of ZrO_2 is much higher than those of YAG and Al_2O_3. Therefore, ZrO_2 is subjected to tensile residual stresses and the Al_2O_3 and YAG phases are often subjected to compressive residual stresses in the Al_2O_3/YAG/ZrO_2 ternary system.[1,50] According to Frazer,[50] the residual tensile stress in ZrO_2 reaches 1.13 GPa in Al_2O_3/YAG/ZrO_2 ternary system. The interaction between the high residual stresses and the propagating cracks is the direct reason for the toughening effect.[12]

From the view of the cracks propagation pattern, the toughening effect of ZrO_2 is characterized by the following aspects. (1) Crack bridging. As observed from the crack path in Fig. 8a, an initial crack is arrested followed by the generation of another parallel crack below the initial crack tip. Such crack bridging can reduce the driving force of crack propagation due to the development of elastic bridges behind the main crack tip. It has been well established that the crack bridging in the crack wake is an effective toughening mechanisms in brittle solids and often responsible for the high toughness.[1,35] (2) Crack deflection. As shown in Fig. 8, the cracks deflect after the contact to the phase interface. The crack deflection paths are shown by the curved arrows "1" in Fig. 8. This phenomenon is consistent with that reported on CaF_2/MgO[51] eutectics produced by the Bridgman method. The crack deflection is a well known toughening mechanism in ceramic matrix composite and considered as the major toughening mechanism in CaF_2/MgO[51] and CoO/YSZ.[52] According to LLorca et al.,[1] the crack deflection is attributed to the presence of fluctuating residual stress fields and the elastic mismatch between the eutectic phases. Furthermore, Faber

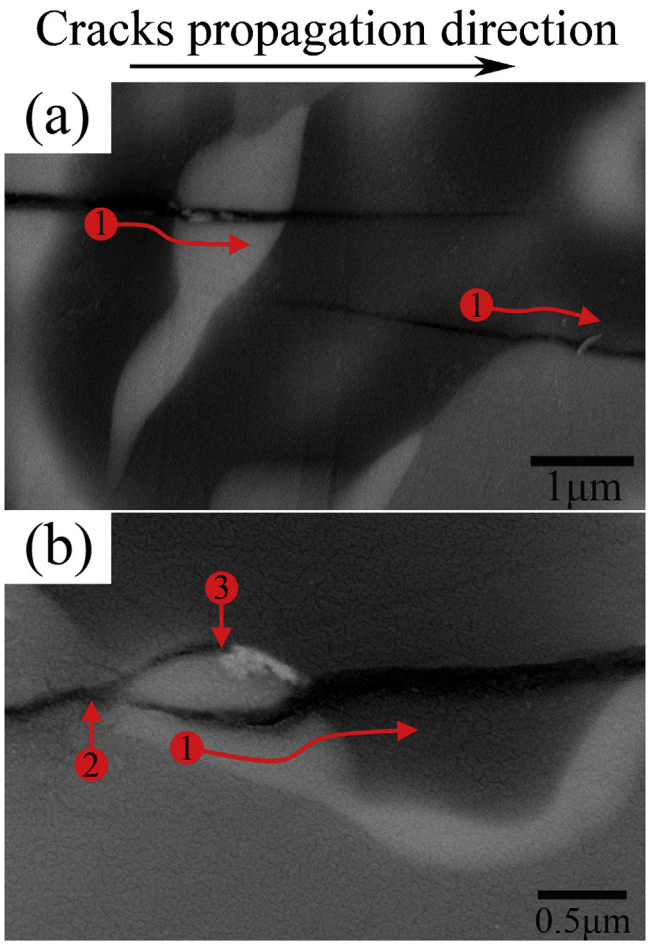

Fig. 8. SEM images showing the indentation cracks propagation pattern in Al_2O_3/YAG/ZrO_2 DSC and the corresponding toughening mechanism: (a) crack bridging and deflection and (b) crack branching and deflection.

et al.[53] have predicted that only the crack deflection around the second phase can lead to a toughness increment of 12–15%. (3) Crack branching. As observed from the crack path in Fig. 8b, the main crack branches into two secondary cracks at the YAG/ZrO_2 interface pointed by the arrow "2". In addition, one of them is arrested (pointed by the arrow "3") after a short propagation along the Al_2O_3/ZrO_2 interface. Another weak crack is initiated nearby to grow as a new main crack. The crack branching would retard the crack growth and reduce crack tip stress intensity, and thus toughen the ceramic.[13] It should be noted that the above three toughening mechanisms were seldom observed in Al_2O_3/YAG binary eutectic system.[1]

4. Conclusion

Al_2O_3/YAG/ZrO_2 hypereutectic DSCs with three compositions are prepared by LFZ method at solidification rate between 2 μm/s and 30 μm/s. The results indicate that:

1. Full lamellar microstructure, free of primary phase, can be obtained from hypereutectic composition by using LFZ method.
2. The YAG phase, coupled with ZrO_2 phase, plays the leading role in the ternary hypereutectic solidification. This result is consistent with Al_2O_3/YAG/ZrO_2 eutectic composition.
3. The minimum lamellar spacing is 1.9 μm, which occurs in AYZ3 sample with a solidification rate of 30 μm/s.
4. The variation tendency of the lamellar spacing is attributed to the changes in both of the thermal and solute transfer condition with different ZrO_2 content.
5. The maximum hardness and fracture toughness are 19.06 GPa and 3.8 MPa $m^{1/2}$, respectively. The fracture toughness increases as ZrO_2 content increased. The toughening mechanism of ZrO_2 is discussed through the crack propagation pattern.

Acknowledgements

Thanks are given to the National Natural Science Foundation of China (51002122, 50772090); New People and New Directions Foundation of School of Materials Science and Engineering in NPU (09XE01045); Research Fund of the State Key Laboratory of Solidification Processing in NPU (76-QP-2011) and the 111 Project (B08040).

The authors wish to thank Dr. Y.Q. Cai from the Institute of High Performance Computing, A*STAR, Singapore for the useful discussion.

References

1. LLorca J, Orera VM. Directionally solidified eutectic ceramic oxides. *Prog Mater Sci* 2006;**51**:711–809.
2. Hirano K. Application of eutectic composites to gas turbine system and fundamental fracture properties up to 1700 °C. *J Eur Ceram Soc* 2005;**25**:1191–9.
3. Waku Y, Sakata S, Mitani A, Shimizu K, Hasebe M. Temperature dependence of flexural strength and microstructure of Al_2O_3/$Y_3Al_5O_{12}$/ZrO_2 ternary melt growth composites. *J Mater Sci* 2002;**37**:2975–82.
4. Fritsch M, Klemm H. The water vapor hot gas corrosion of MGC materials with Al_2O_3 as a phase constituent in a combustion atmosphere. *J Eur Ceram Soc* 2008;**28**:2353–8.
5. Su H, Zhang J, Deng Y, Liu L, Fu H. A modified preparation technique and characterization of directionally solidified Al_2O_3/$Y_3Al_5O_{12}$ eutectic in situ composites. *Scripta Mater* 2009;**60**:362–5.
6. Su H, Zhang J, Liu L, Fu H. Preparation and microstructure evolution of directionally solidified Al_2O_3/YAG/YSZ ternary eutectic ceramics by a modified electron beam floating zone melting. *Mater Lett* 2013;**91**:92–5.
7. Epelbaum BM, Yoshikawa A, Shimamura K, Fukuda T, Suzuki K, Waku Y. Microstructure of Al_2O_3/$Y_3Al_5O_{12}$ eutectic fibers grown by μ-PD method. *J Cryst Growth* 1999;**198–199**:471–5.
8. Lee JH, Yoshikawa A, Fukuda T, Waku Y. Growth and characterization of Al_2O_3/$Y_3Al_5O_{12}$/ZrO_2 ternary eutectic fibers. *J Cryst Growth* 2001;**231**:115–20.
9. Pastor JY, LLorca J, Salazar A, Oliete PB, De Francisco I, Peña JI. Mechanical properties of melt-grown alumina–yttrium aluminum garnet eutectics up to 1900 K. *J Am Ceram Soc* 2005;**88**:1488–95.
10. Peña JI, Larsson M, Merino RI, Francisco ID, Orera VM, LLorca J, et al. Processing, microstructure and mechanical properties of directionally-solidified Al_2O_3–$Y_3Al_5O_{12}$–ZrO_2 ternary eutectics. *J Eur Ceram Soc* 2006;**26**:3113–21.
11. Su HJ, Zhang J, Cui CJ, Liu L, Fu HZ. Rapid solidification behaviour of Al_2O_3/$Y_3Al_5O_{12}$ (YAG) binary eutectic ceramic in situ composites. *Mater Sci Eng A* 2008;**479**:380–8.

12. Su H, Zhang J, Liu L, Fu H. Microstructure and mechanical properties of a directionally solidified $Al_2O_3/Y_3Al_5O_{12}/ZrO_2$ hypoeutectic in situ composite. *Compos Sci Technol* 2009;**69**:2657–67.
13. Su HJ, Zhang J, Cui CJ, Liu L, Fu HZ. Rapid solidification of $Al_2O_3/Y_3Al_5O_{12}/ZrO_2$ eutectic in situ composites by laser zone remelting. *J Cryst Growth* 2007;**307**:448–56.
14. Su HJ, Zhang J, Deng YF, Liu L, Fu HZ. Growth and characterization of nanostructured Al_2O_3/YAG/ZrO_2 hypereutectics with large surfaces under laser rapid solidification. *J Cryst Growth* 2010;**312**:3637–41.
15. Oliete PB, Peña JI, Larrea A, Orera VM, LLorca J, Pastor JY, et al. Ultra-high-strength nanofibrillar Al_2O_3–YAG–YSZ eutectics. *Adv Mater* 2007;**19**:2313–8.
16. Oliete PB, Peña JI. Study of the gas inclusions in $Al_2O_3/Y_3Al_5O_{12}$ and $Al_2O_3/Y_3Al_5O_{12}/ZrO_2$ eutectic fibers grown by laser floating zone. *J Cryst Growth* 2007;**304**:514–9.
17. Ester FJ, Larrea A, Merino RI. Processing and microstructural study of surface laser remelted Al_2O_3–YSZ–YAG eutectic plates. *J Eur Ceram Soc* 2011;**31**:1257–68.
18. Calderon-Moreno JM, Yoshimura M. Al_2O_3–$Y_3Al_5O_{12}$(YAG)–ZrO_2 ternary composite rapidly solidified from the eutectic melt. *J Eur Ceram Soc* 2005;**25**:1365–8.
19. Calderon-Moreno JM, Yoshimura M. Nanocomposites from melt in the system Al_2O_3–YAG–ZrO_2. *Scripta Mater* 2001;**44**:2153–6.
20. Nagira T, Yasuda H, Takeshima S, Sakimura T, Waku Y, Uesugi K. Chain structure in the unidirectionally solidified Al_2O_3–YAG–ZrO_2 eutectic composite. *J Cryst Growth* 2009;**311**:3765–70.
21. Lee JH, Yoshikawa A, Murayama Y, Waku Y, Hanada S, Fukuda T. Microstructure and mechanical properties of $Al_2O_3/Y_3Al_5O_{12}/ZrO_2$ ternary eutectic materials. *J Eur Ceram Soc* 2005;**25**:1411–7.
22. Su HJ, Zhang J, Tian JJ, Liu L, Fu HZ. Preparation and characterization of $Al_2O_3/Y_3Al_5O_{12}/ZrO_2$ ternary hypoeutectic in situ composites by laser rapid solidification. *J Appl Phys* 2008;**104**:23511.
23. Su H, Zhang J, Song K, Liu L, Fu H. Investigation of the solidification behavior of Al_2O_3/YAG/YSZ ceramic in situ composite with off-eutectic composition. *J Eur Ceram Soc* 2011;**31**:1233–9.
24. Zhang J, Su H, Song K, Liu L, Fu H. Microstructure, growth mechanism and mechanical property of Al_2O_3-based eutectic ceramic in situ composites. *J Eur Ceram Soc* 2011;**31**:1191–8.
25. Orera VM, Cemborain R, Merino RI, Peña JI, Larrea A. Piezo-spectroscopy at low temperatures: residual stresses in Al_2O_3–$ZrO_2(Y_2O_3)$ eutectics measured from 77 to 350 K. *Acta Mater* 2002;**18**:4677–86.
26. Alton WJ, Barlow AJ. Temperature dependence of the elastic constants of yttrium aluminum garnet. *J Appl Phys* 1967;**38**:3023–4.
27. Pardo JA, Merino RI, Orera VM, Peña JI, González C, Pastor JY, et al. Piezospectroscopic study of residual stresses in Al_2O_3–ZrO_2 directionally solidified eutectics. *J Am Ceram Soc* 2000;**11**:2745–52.
28. Song K, Zhang J, Jia X, Su H, Liu L, Fu H. Solidification microstructure of laser floating zone remelted Al_2O_3/YAG eutectic in situ composite. *J Cryst Growth* 2012;**345**:51–5.
29. Song K, Zhang J, Jia X, Su H, Liu L, Fu H. Longitudinal cross-section microstructure of growth striation in $Al_2O_3/Y_3Al_5O_{12}/ZrO_2$ directionally solidified eutectic ceramic prepared by laser floating zone. *J Eur Ceram Soc* 2013;**33**:1123–8.
30. Lakiza SM, Lopato LM. Stable and metastable phase relations in the system Alumina–Zirconia–Yttria. *J Am Ceram Soc* 1997;**80**:893–902.
31. Lee JH, Yoshikawa A, Durbin SD, Yoon DH, Fukuda T, Waku Y. Microstructure of Al_2O_3/ZrO_2 eutectic fibers grown by the micro-pulling down method. *J Cryst Growth* 2001;**222**:791–6.
32. Yoshikawa A, Epelbaum BM, Hasegawa K, Durbin SD, Fukuda T. Microstructures in oxide eutectic fibers grown by a modified micro-pulling-down method. *J Cryst Growth* 1999;**205**:305–16.
33. Niihara K. A fracture mechanics analysis of indentation-induced Palmqvist crack in ceramics. *J Mater Sci Lett* 1983;**5**:221–3.
34. Song K, Zhang J, Jia X, Su H, Liu L, Fu H. Microstructure of Al_2O_3/YAG/ZrO_2 eutectic in situ composite prepared by laser floating zone melting. In: *TMS Annual Meeting*. 2012. p. 217–24.
35. Calderon-Moreno JM, Yoshimura M. Microstructure and mechanical properties of quasi-eutectic Al_2O_3–$Y_3A_{l5}O_{12}$–ZrO_2 ternary composites rapidly solidified from melt. *Mater Sci Eng A* 2004;**375–377**:1246–9.
36. Jackson KA, Hunt JD. Lamellar and rod eutectic growth. *Trans Metall Soc AIME* 1966;**236**:1129–42.
37. Gündüz M, Kaya H, Çadırı E, Özmen A. Interflake spacings and undercoolings in Al–Si irregular eutectic alloy. *Mater Sci Eng A* 2004;**369**:215–29.
38. Guzik E, Kopyciński D. Modeling structure parameters of irregular eutectic growth: modification of Magnin–Kurz theory. *Metall Mater Trans A* 2006;**37**:3057–67.
39. Magnin P, Trivedi R. Eutectic growth: a modification of the Jackson and Hunt theory. *Acta Metal Mater* 1991;**39**:453–67.
40. Magnin P, Kurz W. An analytical model of irregular eutectic growth and its application to Fe–C. *Acta Metall* 1987;**35**:1119–28.
41. Jones H, Kurz W. Growth temperatures and the limits of coupled growth in unidirectional solidification of Fe–C eutectic alloys. *Metall Mater Trans A* 1980;**11**:1265.
42. Sato T, Sayama Y. Completely and partially co-operative growth of eutectics. *J Cryst Growth* 1974;**22**:259–71.
43. Liu L, Huang T, Qu M, Liu G, Zhang J, Fu H. High thermal gradient directional solidification and its application in the processing of nickel-based superalloys. *J Mater Process Technol* 2010;**210**:159–65.
44. Khan S, Elliott R. Solidification kinetics of the unmodified aluminium–silicon flake structure. *Acta Metal Mater* 1993;**41**:2433–9.
45. Fisher DJ, Kurz W. A theory of branching limited growth of irregular eutectics. *Acta Metall* 1980;**28**:777–94.
46. Trivedi R, Kurz W. Solidification microstructures: a conceptual approach. *Acta Metal Mater* 1994;**42**:15–23.
47. Magnin P, Kurz W. Competitive growth of stable and metastable Fe–C–X eutectics: Part I. Experiments. *Metall Mater Trans A* 1988;**19**:1955.
48. Mazerolles L, Piquet N, Trichet M, Perrière L, Boivin D, Parlier M. New microstructures in ceramic materials from the melt for high temperature applications. *Aerosp Sci Technol* 2008;**12**:499–505.
49. Tsai SW, Hahn HT. *Introduction to composite materials*. Lancaster: Technomic Publishing Company; 1980.
50. Frazer CS [PhD thesis] *Thermal residual stresses in directionally-solidified alumina–YAG and alumina–zirconia eutectic composites: measurement and modeling*. Elizabeth Dickey, MI: University of Kentucky; 2003.
51. Larrea A, Contreras L, Merino RI, LLorca J, Orera VM. Microstructure and physical properties of CaF_2–MgO eutectics produced by the Bridgman method. *J Mater Res* 2000;**15**:1314–9.
52. Brewer LN, Guruz MU, Dravid VP. Interfacial fracture mechanisms in solid solution directionally solidified eutectic oxide composites. *Acta Mater* 2004;**52**:3781–91.
53. Faber KT, Evans AG. Crack deflection processes –I. Theory. *Acta Metall* 1983;**4**:565–76.